Particle transport and resuspension by shoaling internal solitary waves

David Deepwell,[1,*] Raphaël Sapède,[2] Liam Buchart,[3]
Gordon E. Swaters,[4] and Bruce R. Sutherland[1]

[1]*Department of Physics, University of Alberta, Edmonton, Alberta, Canada T6G 2E1*
[2]*ENSTA ParisTech, Université Paris-Saclay, 91762 Palaiseau Cedex, Paris, France*
[3]*Department of Earth and Atmospheric Science, University of Alberta, Edmonton, Alberta, Canada T6G 2E1*
[4]*Department of Mathematical and Statistical Sciences, University of Alberta, Edmonton, Alberta, Canada T6G 2E1*

(Received 18 October 2019; accepted 6 April 2020; published 7 May 2020)

Particle resuspension due to shoaling internal solitary waves is studied through laboratory experiments and direct numerical simulations. Experiments examine particles placed along the sloping bottom to observe when and where bed load transport and particle resuspension occur. Through a comparison of velocimetry measurements between the experiments and the simulations, the accuracy of the numerical results is established. A suite of simulations is conducted to investigate the dependence of the location of incipient particle resuspension on the bottom slope and incident wave parameters. While a rapid increase in the Shields parameter in the lee of the shoaling wave corresponds to the observed location of resuspension, we find that particle transport away from the bottom is better assessed by the resuspension criterion $w_L/w_s > 1$, where w_s is the particle settling velocity and $w_L = w - su$ is the vertical Lagrangian velocity in which $\vec{u} = (u, w)$ is the Eulerian velocity and s is the slope, which measures the rise of fluid from the bottom following a streamline.

DOI: 10.1103/PhysRevFluids.5.054303

I. INTRODUCTION

Internal solitary waves (ISWs) are a phenomenon studied on account of their common occurrence in lakes [1] and the coastal ocean. Large-amplitude internal waves have been observed in the South China Sea [2–4], north Western Australia [5,6], and the coasts of Oregon and Washington [7–9], among other coastal regions in which these waves shoal and interact with the shelf.

In lakes, a sustained wind stress causes the accumulation of the surface layer at one edge. Upon the relaxation of the wind, an internal seiche forms and degenerates into a train of ISWs because of nonlinear steepening [10]. Therefore, ISWs are a fundamental mechanism for the transfer of energy from basin-scale to small-scale motions through their adjustment due to bottom topography [11]. This cascade to smaller scales often leads to the mixing of surface and deep waters, material transport, and the redistribution of biogeochemical constituents which dramatically impacts the biological productivity of the lake [12].

During shoaling, the structure of the wave adjusts to the changing background fluid depth and will eventually break, resulting in dissipation of incident wave energy. Particle resuspension due to shoaling internal solitary waves has been frequently observed [13–18], causes changes in water chemistry [19], and is suggested to have formed nepheloid layers [4,15].

*deepwell@ualberta.ca

Though shoaling internal waves have been studied for many years, there is still a gap in our understanding of where resuspension occurs during the shoaling process [18]. Because shoaling waves repeatedly apply stress near the same position, the erosion they induce may be problematic. For offshore structures, in particular for pipelines that lie on the ocean floor between offshore drilling sites and onshore refineries near north Western Australia, this could be of concern. These pipelines extend from below to above the thermocline, and so a shoaling wave is likely to resuspend sediments underlying the pipeline, thereby weakening its foundations.

Particle transport consists of a variety of stages. First, unconsolidated particles slide and roll under the action of the surrounding fluid motion, through what is called bed load transport. Saltation develops at higher flow velocities before transitioning into sustained particle suspension. At still higher flow velocities, turbulent eddies can be important for initiating particle motion and keeping them in suspension. Pioneering work on categorizing these regimes was done by Shields [20]. A nondimensionalized parameter, which now bears his name, compares the bed stress to the buoyancy per area of an individual particle. However, this diagnostic was developed for unidirectional quasisteady flows as opposed to the transient flows associated with a shoaling internal solitary wave.

Extensive laboratory and numerical studies of shoaling ISWs have been used to classify wave breaking [21–23] and discussed flow separation and global instabilities in the bottom boundary layer during shoaling [24,25]. Boegman and Ivey [26] showed that bottom viscous stresses were incapable of predicting resuspension and emphasized the importance of near-bed Reynolds stress. On shallow slopes, shoaling internal solitary waves transform into upslope traveling boluses which transport material onshore while also creating intermediate nepheloid layers [15,27,28]. Sutherland *et al.* [29] developed simple heuristics for different flow features during shoaling such as the maximum interfacial descent, and the speed and range of the upslope bolus. However, although particle resuspension and bed load transport were observed, the conditions leading to transport were not quantified.

Here we report upon laboratory experiments and numerical simulations that let us formulate a prediction for the location of resuspension caused by shoaling internal solitary waves. The experimental methodologies with qualitative results are discussed in Sec. II. Quantitative results of the laboratory experiments are presented in Sec. III. Section IV introduces numerical simulations comparable to the experiments as well as simulations that lead to a predictive criterion for resuspension. A concluding discussion is given in Sec. V.

II. EXPERIMENT SETUP AND QUALITATIVE RESULTS

Here we present the experimental configuration in addition to snapshots, time series images, and velocimetry data of a typical experiment. Also described are analysis methods used to determine quantitative results.

A. Experiment setup

Laboratory experiments of shoaling internal solitary waves were conducted to examine waves at different amplitudes approaching a range of bottom boundary slopes. Extending previous shoaling experiments [29], relatively large, moderate density particles (mustard seeds, $D_p \approx 0.1$ cm) were placed along the bottom boundary to enable the visualization of bed load transport and particle resuspension.

In each experiment a single internal solitary wave of depression was generated in a two-layer salt-stratified fluid through a standard lock-release mechanism. The tank was 197.3 cm long, 17.4 cm wide, and 49 cm high; the length is sufficiently long for a wave to form before significant shoaling begins. For simplicity of the setup, the tank was tilted at an angle θ so that the resultant wave shoaled directly onto the base of the tank (Fig. 1). The tilt angle ranged between $\theta = 2.0^\circ$ and 9.8°, giving a range of slopes between $s = 0.035$ and 0.173. This is comparable to slopes at an ocean shelf [30,31]

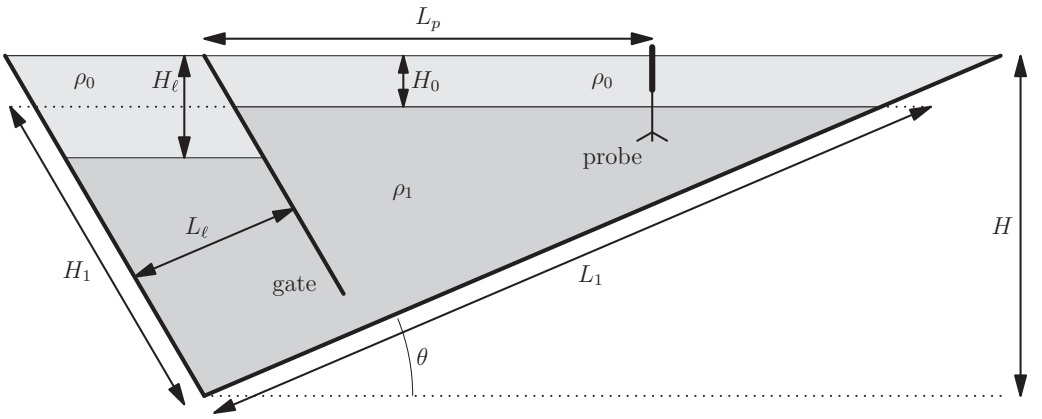

FIG. 1. Initial tank configuration showing variables defining the layer depths, densities, and position of the probe (diagram not to scale).

which can vary between 0.02 in Louisiana and the Niger Delta to 0.17 in the Bay of Biscay. Lakes can have slopes [21,32,33] in the range of 0.01–0.05.

The ambient stratification consisted of two miscible layers: a saline layer underneath a shallow fresh layer. The depth of the upper fresh layer H_0 was approximately 2 cm for all experiments. Once the background stratification was formed, a removable gate was inserted a distance $L_\ell = 18.5$ cm from the end wall to form a lock. A gap of a few centimeters was left between the bottom of the gate and the tank. The upper layer depth was gradually increased behind the gate by slowly adding fresh water through a sponge float until the upper layer reached a depth of H_ℓ which varied between 4.2 and 29.6 cm. This lock depth set the resultant wave amplitude and determined the energetics of the wave shoaling. The maximum fluid depth was approximately 36 cm and the density difference $\Delta\rho = \rho_1 - \rho_0$ ranged between 0.020 and 0.076 g/cm^3.

Mustard seeds were then sprinkled across the surface of the tank to form a dilute layer on the bottom slope. Most of the mustard seeds settled to the bottom of the tank, while some remained on the surface of the fresh layer and some remained on the interface between the two layers. These suspended particles have minimal impact on the shoaling wave because there are so few of them. That the particles settled over a range of depths is a consequence of the seeds having a range of densities affected in part by water absorption. As most of the mustard seeds were slightly heavier than the surrounding water, they acted as weak inertial particles. In the context of our experiments, mustard seeds can be considered cohesionless, especially since the particle fraction was low to minimize particle-particle interactions.

An individual experiment was initiated with the rapid removal of the gate causing the deep upper layer fluid originating behind the gate to collapse into the ambient shallow upper layer forming a single internal solitary wave of depression. After the first experiment was completed and the ambient fluid was again stationary, the removable gate was inserted and fresh water was siphoned from the ambient until the upper layer returned to a depth of H_0. More fresh water was then added behind the gate to create a lock depth greater than that in the first experiment. Typically, the background stratification was used twice in repeat experiments with different values of H_ℓ. At high tilt angle, the stratification was occasionally reused four times.

Experiments were recorded by a Canon Rebel T3I camera which was placed 300 cm in front of the tank and centered on the middle of the tank. The recorded movies were then analyzed in MATLAB to measure the amplitude, speed, and wavelength of the wave as well as to extract time series of near-bottom particles.

A vertically scanning Nortek Vectrino velocimetry probe measured the three components of velocity near the bottom slope. The probe was placed midway between the two sidewalls of the

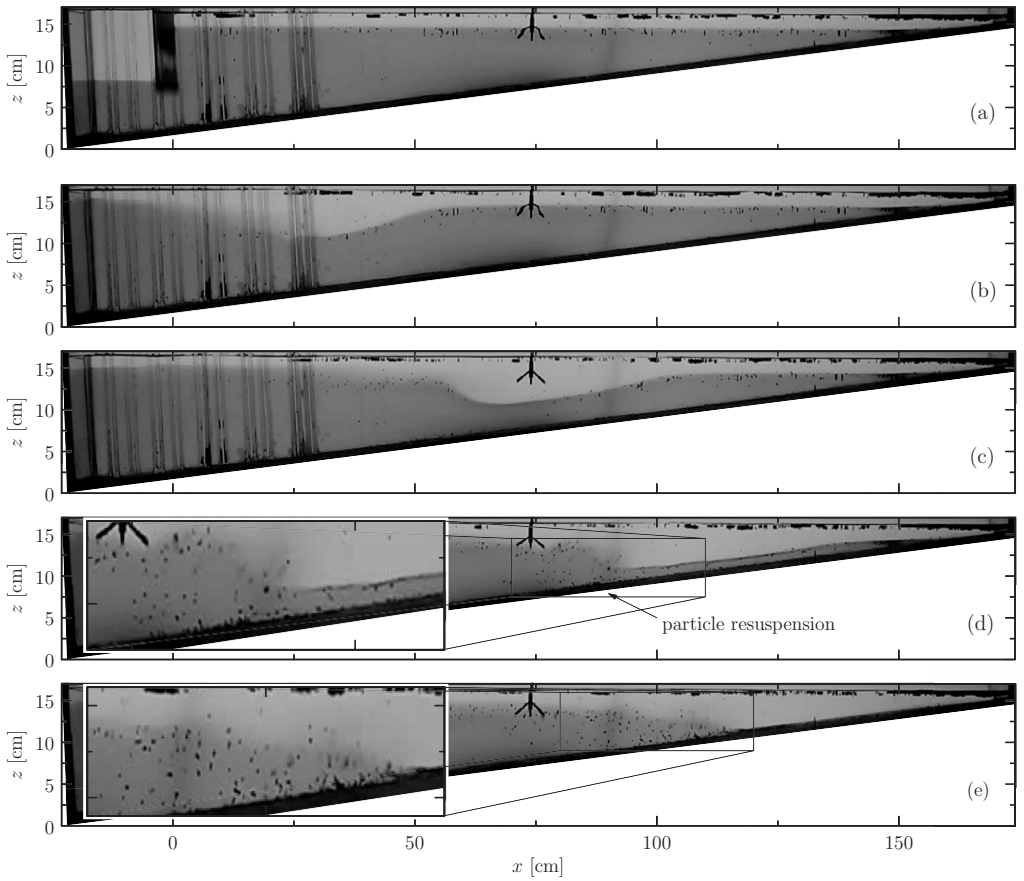

FIG. 2. Successive snapshots (from [34]) from experiment with bottom slope $s = 0.084$ and $H_\ell = 9.6$ cm (wave amplitude of $A_{sw} = 5.1$ cm) at (a) $t = 0$ s, (b) $t = 5$ s, (c) $t = 10$ s, (d) $t = 15$ s, and (e) $t = 20$ s. Slanted grooves in the left section of the tank are guides for the gate and do not impact the wave formation in any significant way. A Vectrino velocimetry probe is seen at $x = 75$ cm.

channel approximately 7 cm above the local tank bottom and recorded velocities at 100 Hz between the bottom and 3.5 cm above the bottom with a resolution of 1 mm. In repeat experiments with nearly identical initial conditions, four primary locations for the probe position (as measured from the gate location at the surface) were used, $L_p = 40, 60, 80, 100$ cm, to measure the velocity while the wave approached, shoaled, and transformed into a bolus. The presence of the probe did not appear to impact the shoaling internal wave in any significant way as evident from nearly identical breaking behavior in repeat experiments, independent of probe position.

B. Qualitative results

The time evolution of the formation, propagation, and shoaling of an internal wave for a typical experiment is shown by successive snapshots in Fig. 2. The experiment began with the rapid removal of the gate, which enabled the collapse of the deeper upper layer behind the gate [Fig. 2(a)]. This collapsing lock fluid transformed into a single internal solitary wave within a short distance [Fig. 2(b)]. Although this wave may not have been fully adjusted into a canonical internal solitary wave due to the shortness of the tank, we anticipated that the resuspension would be unaffected by this because the shoaling necessarily modified the wave into a particular form for the slopes

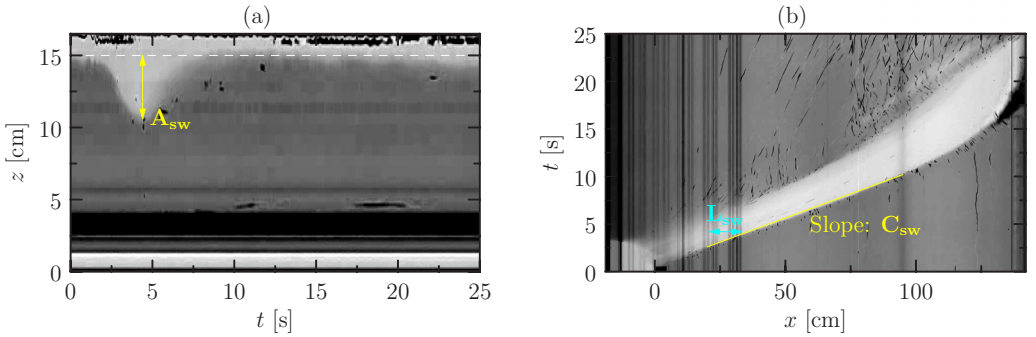

FIG. 3. (a) Vertical time series taken at $x = 21$ cm and (b) horizontal time series taken at the depth of the half maximum wave amplitude taken from the experiment shown in Fig. 2. The amplitude A_{sw}, wave speed C_{sw}, and wavelength L_{sw} of the ISW are defined from these cross-sectional time series. The dashed line in (a) indicates the location of the initial ambient fluid interface. Because the tank is tilted, the bottom of the tank at $x = 21$ cm is at $z = 4$ cm in (a).

used in this study [Fig. 2(c)]. The solitary wave sometimes had interfacial mixing in the wave's lee, a consequence in part of the gate extraction. In all experiments, particles experienced bed load transport as a result of the wave-induced velocities.

As the wave shoaled, the leading flank of the wave flattened to become parallel to the bottom slope, while the rear flank of the wave gradually steepened [Fig. 2(c)]. This rear steepening and leading flattening continued as the interface was drawn down towards the bottom slope such that the shoaling wave began to appear triangular. Breaking typically occurred approximately when the rear flank of the wave steepened to nearly vertical, corresponding to the maximum vertical interfacial drawdown. While bed load transport was always observed below the flattening wave front, no particle resuspension was observed there. Rather, particles were resuspended near the rear of the wave around the time of breaking [Fig. 2(d)]. These particles were carried vertically away from the bottom near the location of maximum interfacial drawdown. Thereafter, a bore formed which carried some resuspended particles back upslope as it further transformed into a bolus [Fig. 2(e)]. Greater emphasis on the bolus formation and associated particle resuspension can be found in the work of Moore *et al.* [35] and Tian *et al.* [36], respectively. Most of the incident wave energy dissipated during shoaling since very little wave reflection was observed [Fig. 2(e)].

The incident wave properties are determined from two separate time series constructed from movies of the experiments. A vertical time series was constructed from the combination of successive vertical cross sections 21 cm from the gate [Fig. 3(a)]. From this, the wave amplitude A_{sw} was measured as the maximum vertical displacement of the interface. A horizontal time series was then constructed from successive horizontal cross sections at a depth $H_0 + A_{sw}/2$ [Fig. 3(b)]. From this, the wave speed C_{sw} and horizontal extent L_{sw} were measured [Fig. 3(b)]. The wave speed was found from the slope of a linear fit of the leading wave front from formation until the wave experienced a deceleration due to shoaling. Typically, the speed was found to be constant from the point of formation up to 100 cm from the gate. The horizontal extent L_{sw} was measured as the distance between the leading flank at depth $A_{sw}/2$ below the interface and the position of maximum interfacial descent when the wave is 21 cm from the gate.

Figures 3(a) and 3(b) show that the interface returned to the initial ambient interface depth with no secondary waves being observed to trail the solitary wave formed by the lock release. The wave traveled at a constant speed until decelerating during shoaling [$t > 10$ s in Fig. 3(b)]. Particle resuspension is evident by the dark speckles behind the wave around $t = 15$ s.

To examine bed load transport, a diagonal time series was constructed by combining successive cross sections parallel to the bottom slope at a distance 0.1 cm, approximately a particle diameter,

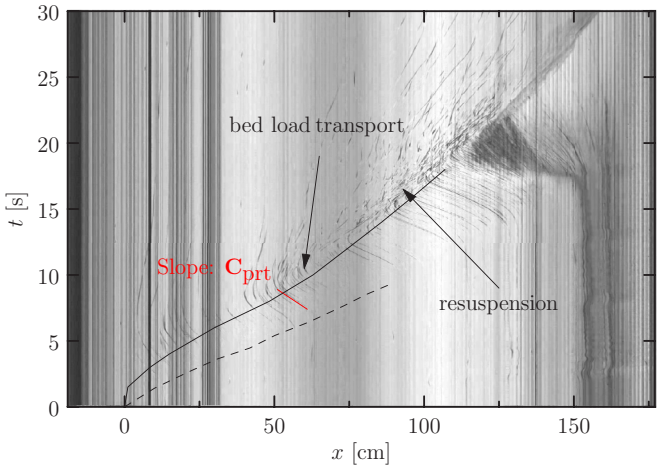

FIG. 4. Diagonal time series taken along a cross section 0.1 cm above the bottom slope. Bed load transport is apparent by the streak marks made by individual particles. The initial conditions are the same as those in Figs. 2 and 3. The black solid line denotes the location of the wave at its deepest point and the black dashed line shows the location of the wave front along which C_{sw} was calculated.

above the tank bottom (Fig. 4). The black line shows the location of maximum interfacial descent which indicates the position of the wave. The diagonal time series shows particles moving downslope (leftward) ahead of the wave before reversing direction as a result of the adverse pressure gradient associated with near bottom boundary motions induced by internal solitary waves [24–26,37,38]. The adverse pressure gradient (also called a prograde jet) is a region within the boundary layer where the horizontal velocity is oriented in the same direction as the traveling ISW. As the wave shoaled, the adverse pressure gradient grew in size and strength until particle resuspension began. The movies (see video 1 in the Supplemental Material [34]) showed particle resuspension to occur between approximately $t = 12$ and 21 s where the particle tracks are more scattered, as shown in Fig. 4. Rapid interfacial drawdown near the bottom occurs near the end of resuspension. Thereafter, the interface gradually advanced back upslope. This was associated with the front of a bolus of dense fluid which carried some particles with it.

Although the bed load transport of particles may adjust the boundary layer, we expect this effect to be minimal in our experiments because the particles are fairly dilute and nearly neutrally buoyant. We estimate that the particle diameter is less than the boundary layer thickness $L_{sw}/\sqrt{\mathrm{Re}}$ by a factor of 2. Because these are comparable, the particles may be more susceptible to the interior flow. We anticipate that larger or more dense particles would cause resuspension to be hindered and likely occur later.

Besides movies of the experiments, velocities were measured by a Vectrino probe. Figure 5 shows the horizontal u and vertical w velocity profiles at $x = 100$ cm for the case with $s = 0.085$ and $H_\ell = 9.6$ cm. In many experiments, the probe data were contaminated by noise, in part due to the presence of large particles. The measurements shown in Fig. 5 were contaminated by noise primarily over the bottom 1 cm. Because the probe was situated 35 cm to the right of the resuspension location, the signal was contaminated less by the resuspension of the mustard seeds which had mostly settled.

Before $t = 8$ s, the fluid was nearly stationary with any signals being associated with noise. Shortly after, significant flows developed having negative horizontal and vertical velocities. Until $t = 10$ s, the ratio of these velocities near the bottom approximately equaled the bottom slope $s = 0.085$. The positive (rightward) motion of the core of the solitary wave became evident after $t = 11$ s when the interface descended within the range of the probe. At approximately $t = 15$ s, both velocity components suddenly changed sign as the now large adverse pressure gradient below the rear flank

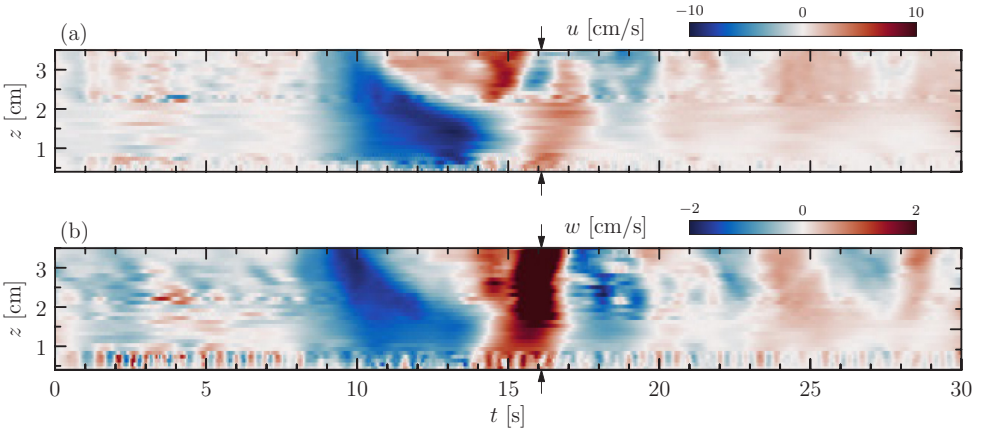

FIG. 5. (a) Horizontal and (b) vertical velocities as measured by the probe 100 cm from the gate for experiment with slope $s = 0.085$ and $H_\ell = 9.6$ cm ($A_{sw} = 5.2$ cm). The vertical axis is measured relative to the local base of the tank. Arrows indicate the time for initiation of particle resuspension. Note that the color scales are different for each plot.

of the wave passed the probe. The vertical velocity became as large as 5 cm/s within 2 cm of the bottom at $t = 16$ s. After the wave passed, the velocities returned to small values with some evidence of weak periodic motion possibly associated with wave reflection, although significant periodic displacement of the interface was not evident from movies of this experiment.

III. QUANTITATIVE RESULTS

In all, 89 experiments were performed and analyzed. Here we summarize the collective properties of the incident solitary wave generated by lock release and the shoaling dynamics.

A. Solitary-wave properties

Though the bottom boundary is not horizontal where the ISW was generated, the lower layer was sufficiently deep near the lock that the sloping bottom did not significantly impact the generation of the wave in comparison with experiments on a horizontal bottom [29]. The wave amplitude A_{sw}, measured as shown in Fig. 3(a), is plotted in Fig. 6(a) against the depth of the fluid behind the gate. We have nondimensionalized A_{sw}, L_{sw}, and $H_\ell - H_0$ with the harmonic mean of the two layer depths

$$\bar{H} = \frac{H_0(H - H_0)}{H},$$

where H is the vertical distance from the lowest point of the tank to the fluid surface. This scale is used because, in the theory for small-amplitude interfacial waves, the shallow wave speed is $C_0 = \sqrt{g'\bar{H}}$, where $g' = g(\rho_1 - \rho_0)/\rho_1$ is the reduced gravity.

The wave amplitude is found to depend linearly upon the lock depth according to the relation

$$A_{sw} = 0.596(\pm 0.005)(H_\ell - H_0), \tag{1}$$

showing that the size of the resultant wave is set by the depth of the fluid behind the gate. This relationship is quantitatively different from that reported by Sutherland *et al.* [29], who found $A_{sw} = 0.45(\pm 0.02)(H_\ell - H_0)$. This discrepancy is likely attributed to the fact that the total fluid depth in their experiments was approximately half the depth of our experiments, which poses a restriction on the maximum amplitude. Because the majority of the waves in our experiments had amplitudes larger than H_0, they cannot be described by Korteweg–de Vries theory.

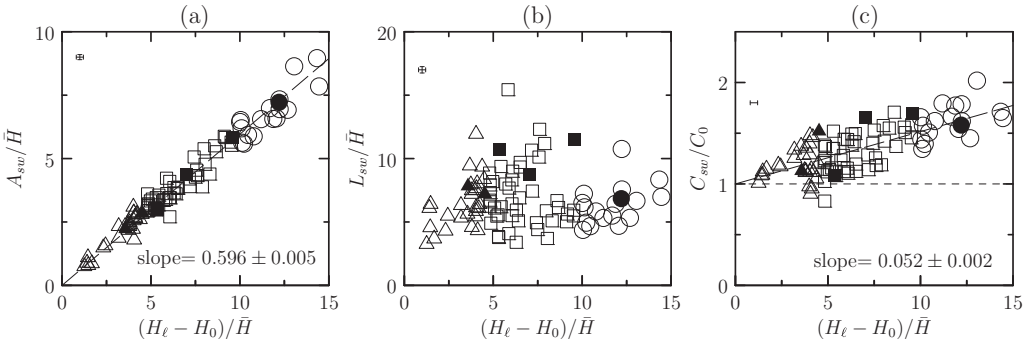

FIG. 6. Relative (a) amplitude, (b) wavelength, and (c) speed of the incident solitary wave versus the scaled lock depth. Symbols denote initial lock conditions: △, $(H_\ell - H_0)/\bar{H} < 5$; □, $5 \leqslant (H_\ell - H_0)/\bar{H} < 10$; and ◯, $(H_\ell - H_0)/\bar{H} \geqslant 10$. Simulation results are shown by closed symbols and typical error bars are shown in the top left of each plot.

Despite some scatter, the wavelength $L_{\rm sw}$ had no clear dependence on the lock depth as shown in Fig. 6(b). Its mean value for all experiments was $6.7(\pm 2.2)\bar{H}$, with the variability largely attributable due to measuring the wavelength early in the wave formation. We expect that the variability in the wavelength will have negligible impact on the resuspension dynamics since the wave continues to adjust during shoaling before particle resuspension occurs. Although we note that Sutherland *et al.* [29] found that two internal waves were formed with a longer lock, the dependence of $L_{\rm sw}$ upon initial conditions was not explored as it goes beyond the focus of our study.

As is common for large-amplitude ISWs, the wave speed was consistently larger than the shallow water speed C_0. The speed increased with lock depth at an approximately linear rate of

$$C_{\rm sw}/C_0 = 1 + 0.052(\pm 0.002)(H_\ell - H_0)/\bar{H},$$

which agrees well with the observations of Sutherland *et al.* [29]. Because the amplitude also scales linearly with lock depth, there is a linear relationship between the wave speed and amplitude

$$C_{\rm sw}/C_0 \simeq 1 + 0.087(\pm 0.003)A_{\rm sw}/\bar{H}.$$

Although the wave amplitude coefficient is smaller than that expected from Korteweg–de Vries theory, it is comparable to that found by Sutherland *et al.* [29]. The discrepancy is likely caused by the lack of adjustment time for the wave to fully form into an internal solitary wave. Because the wave continued to deform before particle resuspension began, an approximate measure of the incident wave is sufficient.

B. Shoaling properties

Breaking typically occurs when the rear flank of the wave steepens to nearly vertical, which corresponds to the maximum vertical interfacial drawdown. Sutherland *et al.* [29] found a simple relation between the maximum vertical drawdown and the incident wave area to be

$$H_i^* = \sqrt{4sA_{\rm sw}L_{\rm sw}},$$

where H_i^* is the predicted maximum interfacial drawdown. This relation arises from an equivalence in the cross-sectional area of a wave at deep and shallow depths.

Figure 7 plots the observed maximum vertical interfacial displacement H_i against the predicted value H_i^*. Our experiments show that the prediction overestimates the observed displacement, especially for waves shoaling on steep slopes ($s > 0.1$). However, this geometric description of the

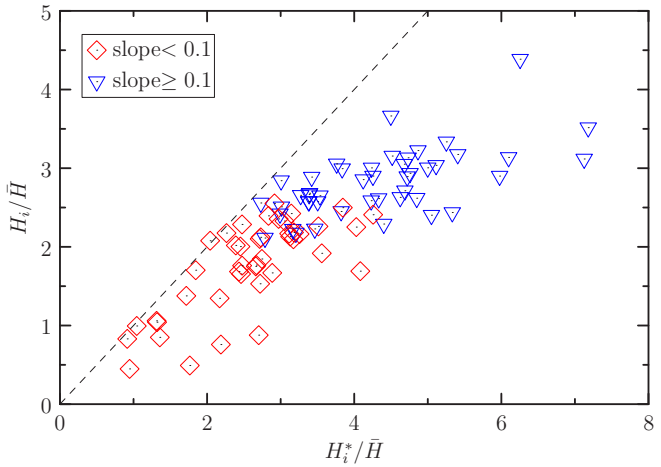

FIG. 7. Observed maximum vertical interface displacement H_i as a function of the predicted displacement H_i^*. The dashed line indicates equal observed and predicted displacements.

shoaling may need to be modified at very shallow slopes where the incident wave fissions during shoaling rather than plunges or surges.

From the near-bottom diagonal time series, such as that shown in Fig. 4, the downslope particle velocities undergoing bed load transport below the leading flank of the shoaling wave were calculated from the displacement versus time of the particle tracks. Figure 8 shows the relation between the particle speed C_{prt} and the measured incident solitary-wave speed C_{sw}. Despite some scatter, the figure shows that the particle speed is generally larger if the approaching wave speed is larger, the downslope speed being about 63% of the incident wave speed. In general, waves were generated with larger amplitudes in experiments with steeper slopes, and therefore larger wave and particle speeds were observed in these cases.

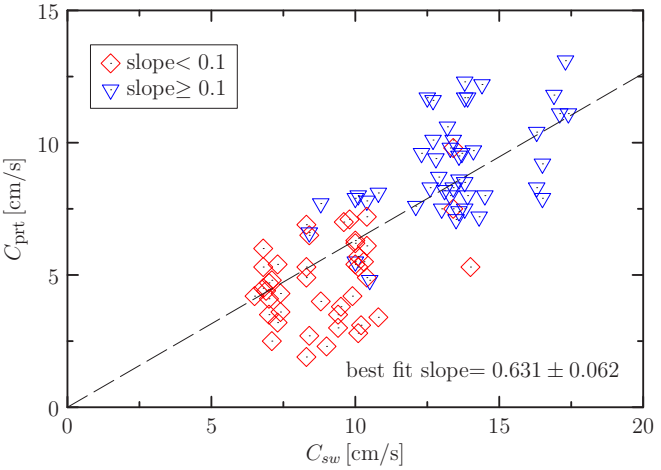

FIG. 8. Particle bed load transport speed C_{prt} versus the incident shallow water wave speed C_{sw}.

IV. NUMERICAL SIMULATIONS OF EXPERIMENTS

Bed load transport and resuspension of particles were observed in the experiments as a consequence of wave-induced motion near the bottom of the tank. Although the experiments revealed the location of resuspension, the velocimetry probe could not accurately measure flow within the bottom 1 cm of the tank and so could not assess the bottom stress. To overcome this deficiency, numerical simulations were performed to provide detailed information about the fluid velocity near the bottom. Movie snapshots and the velocimetry probe data were used to demonstrate the accuracy of the simulations.

Below, after describing the numerical model and demonstrating its validity by comparison with experiments, we diagnose the bottom stress to evaluate the Shields parameter which has been used to predict the onset of bed load transport and resuspension in quasisteady unidirectional flows. The predictions made by the numerical simulations are compared with experiments. Arguing that the Shields parameter does not fully capture the dynamics of particle resuspension due to transiently breaking ISWs, we derive a criterion for resuspension based upon the local near-bed Lagrangian fluid velocities and compare the prediction with observed location of resuspension in experiments.

A. Numerical methods

The scale of the laboratory experiments was small enough to allow direct numerical simulations to be completed. This is particularly useful for accurately modeling the boundary layer dynamics without the use of a turbulence scheme. Here we focus on directly measuring and observing near-bottom velocities and separation which the experiments were unable to measure accurately.

We have conducted both two-dimensional (2D) and 3D simulations with conditions equivalent to the laboratory experiments. Two-dimensional simulations are far cheaper computationally than 3D simulations, but will be seen to be accurate only until shortly after wave breaking occurs (see [22,27]). Fully 3D simulations are used to compare against the laboratory experiments and to explore the fully developed breaking processes.

Simulations were completed with the Spectral Parallel Incompressible Navier-Stokes Solver [39], which has been regularly applied to laboratory conditions such as those above using the Boussinesq approximation. Similar to the configuration of the tank in the laboratory experiments, the computational domain was "tilted" by adjusting the orientation of the gravitational force while mapping the upper surface so that it lies perpendicular to the direction of gravity, i.e., horizontal. The full domain and initial density configuration can be seen in Fig. 9(a).

No-slip boundary conditions were prescribed on the lower and upper boundaries. Ideally, the upper boundary would have a no-shear boundary condition, but this is currently not possible within the numerical model. Even though an unphysical upper boundary condition was used, the agreement with the laboratory experiments regarding the measured incident wave speed, wavelength, and amplitude was excellent, within 10% for all completed cases (see closed symbols in Fig. 6). To cluster points in the boundary layer and to maintain the accuracy of the spectral method used in the model, a Chebyshev grid was used in the vertical. Free-slip conditions were used on all other boundaries. Although laboratory experiments have sidewall friction which, to a small degree, reduces wave energy, because the tank was relatively short, 197.3 cm, this impact was negligible compared to that of the shoaling.

The model used a variable third-order Adams-Bashforth scheme for the time stepper. A typical time step was on the order of 1 ms. Though this is small, the model was still efficient in that 2D simulations were completed in approximately 8 h when running in parallel with eight processors, while 3D simulations took around 2–3 days with eight processors. A variety of resolutions were used in the simulations, the most common being $(\Delta x, \Delta z_{\max}) \approx (0.2\text{ cm}, 0.2\text{ cm})$ in two dimensions and $(\Delta x, \Delta y, \Delta z_{\max}) \approx (0.4\text{ cm}, 0.2\text{ cm}, 0.2\text{ cm})$ in three dimensions. Greater resolution ($\Delta z \approx 10\ \mu$m) near the bottom boundary was achieved by the use of a Chebyshev grid in the vertical dimension.

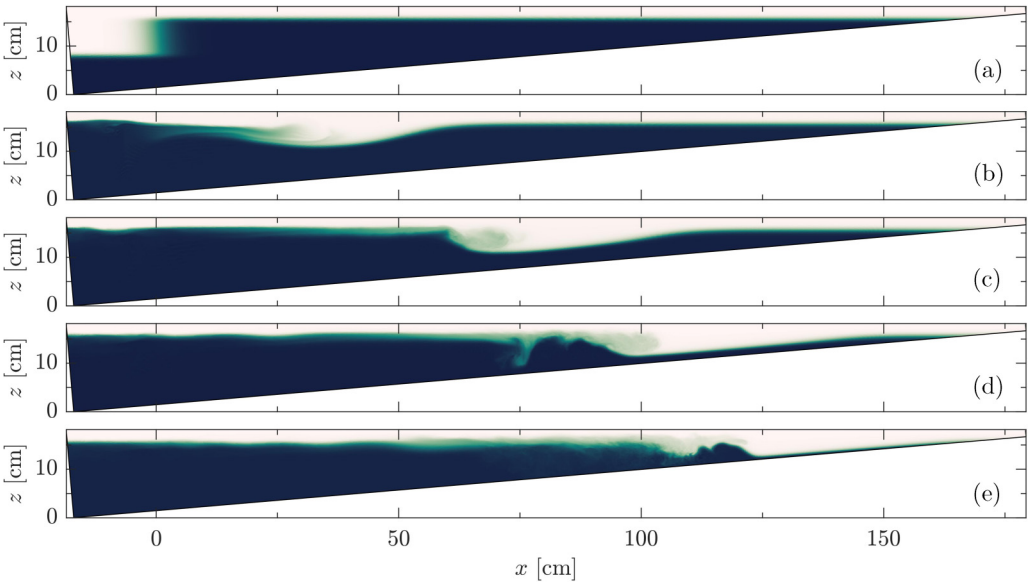

FIG. 9. Snapshots (from [34]) of the density field of a 3D simulation with slope $s = 0.085$ and $H_\ell = 10.2$ cm at (a) $t = 0$ s, (b) $t = 5$ s, (c) $t = 10$ s, (d) $t = 15$ s, and (e) $t = 20$ s. The wave amplitude was $A_{\rm sw} = 4.8$ cm.

The background density field was prescribed as a hyperbolic tangent profile with an interface thickness of 1 cm. For 3D simulations, the initial motionless velocity field was seeded with random white noise on the order 1 mm/s to allow three-dimensional motion to develop.

Simulations had a wave Reynolds numbers $\mathrm{Re}_w = C_0 A_{\rm sw}/\nu$ in the range 2300–6000, which is comparable to the experiments which were between 1000 and 16 000. Although this is significantly smaller than Reynolds numbers in lakes, $\mathrm{Re}_w = 10^6$, and in the ocean, $\mathrm{Re}_w = 10^7$, this is not a significant issue since we are interested in the initialization of resuspension as caused by the form of wave breaking rather than turbulent instabilities within the bottom boundary layer. Furthermore, Aghsaee *et al.* [22] demonstrated that although the Reynolds number modifies the breaking process, it does not change the location of flow separation.

Simulations had a Schmidt number of $\mathrm{Sc} = \nu/\kappa = 10$. Although this is significantly smaller than that for a salt-stratified fluid, its influence upon wave formation and shoaling in such a short domain is negligible. A case with $\mathrm{Sc} = 1$ provided similar boundary layer behavior to the matching case with $\mathrm{Sc} = 10$. The primary difference was that the overturns in the wave aft were smoothed out, but this did not affect wave breaking or flow separation. Yet another case with $\mathrm{Sc} = 1$ and a wave Reynolds number increased by a factor of 5 demonstrated that while the boundary layer was thinner, the underlying dynamics of wave breaking was qualitatively similar.

B. Numerical results

Figure 9 presents snapshots of a 3D simulation with bottom slope $s = 0.085$ and $H_\ell = 10.2$ cm. As in the experiments, a single solitary wave formed with amplitude $A_{\rm sw} = 4.8$ cm. The wave then shoaled [Fig. 9(c)], broke [Fig. 9(d)], and transformed into an upslope traveling bolus [Fig. 9(e)].

For comparison with the experimentally measured velocities, Fig. 10 shows vertical profiles of the horizontal and vertical velocities at $x = 100$ cm during shoaling as determined by the 2D and 3D simulations run with the same initial conditions as the experiments with velocity profiles shown in Fig. 5. As in the experiments, the vertical profiles were extracted at the probe location $x = 100$ cm. The velocities in the 2D and 3D simulations have the same structure and magnitude

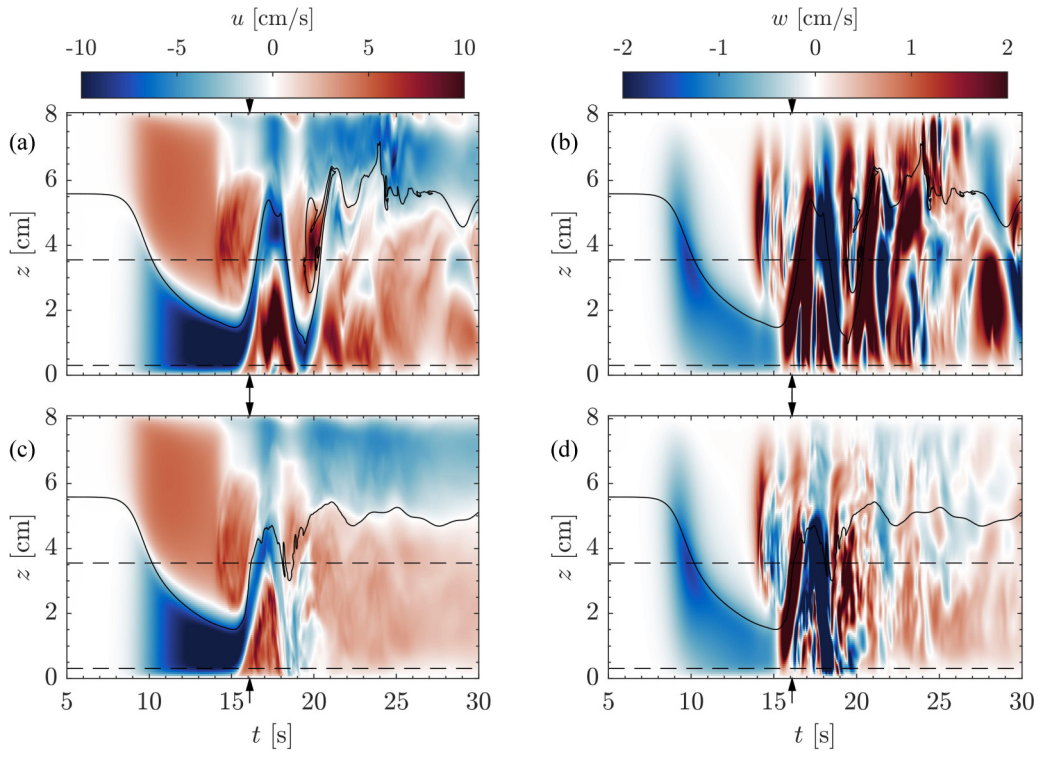

FIG. 10. (a) and (c) Horizontal velocity and (b) and (d) vertical velocity along the vertical cross section at model probe position $x = 100$ cm for (a) and (b) a two-dimensional run and (c) and (d) a three-dimensional run. Horizontal dashed lines correspond to the vertical extrema of the probe data from the experiment (see Fig. 5). The black solid curve is the location of the pycnocline and the arrows indicate the time of particle resuspension as measured in the experiments at this probe location. The vertical axis is measured relative to the local base of the tank.

until approximately $t = 18$ s, after which the wave has passed the probe location and the trailing motion became chaotic (see the Supplemental Material [34] for a video of instantaneous vorticity field). Although the Reynolds numbers are somewhat low, the 3D simulation better modeled the energy cascade to small scales. As such, the motion remained more energetic and coherent in the 2D case than in three dimensions.

Until $t = 15$ s, the vertical and horizontal velocity profiles in the 2D and 3D simulations had similar structures corresponding to near-uniform downslope flow below the pycnocline. Above the pycnocline, the flow within the wave was initially laminar, having a constant positive horizontal velocity and near-zero vertical velocity. After $t = 15$ s, the flow near the boundary reversed direction and the flow aloft was more energetic due to wave breaking. The flow separation at $t = 15$ s occurred within a 0.4-cm-thick bottom boundary layer. At this probe location the flow separation caused fluid to rise 4–5 cm above the bottom before returning to the bottom. Corresponding experiments observed particle resuspension at $t \approx 16$ s (indicated by the vertical arrows in Fig. 10) which occurred after the passage of the separation point.

The simulated velocities between $z = 0.4$ and 3.5 cm, in comparison with the corresponding experiment measurements (Fig. 5), showed excellent agreement up to and shortly after the time of breaking. Notably, the lower layer thinned at approximately the same rate and the flow direction reversed at the same time.

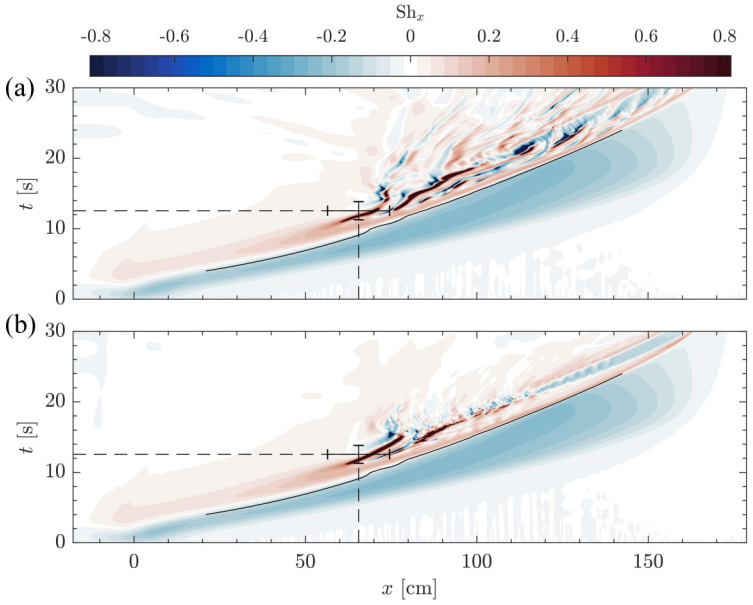

FIG. 11. Along-slope Shields parameter Sh_x for (a) 2D and (b) 3D simulations (where the stress τ_x is in the along-tank direction in the middle of the tank) for the case in Fig. 9. The black point with error bars designates the experimental time and position of incipient resuspension. The black curve is the location of maximum interfacial descent, i.e., the location of the wave.

These results show that the simulations reliably capture the flow dynamics in the experiments. Thus we can accurately capture the stress induced by the shoaling wave acting on the bottom. Furthermore, because the 2D and 3D simulations are quantitatively similar up to and shortly after breaking occurs, the computationally cheaper 2D simulations are sufficient for the analyses that follow.

C. Bed load transport criterion

A common parameter used in sediment transport and resuspension studies is the Shields parameter, which compares the along-channel bed shear stress τ to the weight per area of the particles

$$\mathrm{Sh} = \frac{\tau}{gD(\rho_p - \rho_1)}, \tag{2}$$

in which D is the mean particle diameter and ρ_p and ρ_1 are the densities of the particle and surrounding fluid, respectively [40]. As assessed by a combination of the Shields parameter and particle Reynolds number $\mathrm{Re}_p = u_* D/\nu$, where u_* is the near-bed velocity, experiments and observations of a turbulent, quasisteady, unidirectional flow show that particle motion can be realized as bed load transport recognized by rolling and/or sliding of particles or as suspension characterized by particles remaining within the water column. In particular, an approximate critical Shields parameter for bed load transport [20] is $\mathrm{Sh}_c = 0.1$.

Though the simulations did not contain individual particles, our calculation of Sh from the numerical results used a particle diameter and density of $D = 0.1$ cm and $\rho_p = 1.05$ g/cm^3, respectively. These are approximate values for the mustard seeds used in the laboratory experiments. However, we find that our results are not particularly sensitive to the choice of D and ρ_p. Figure 11 displays an along-slope time series plot of the along-slope Shields parameter Sh_x. In 3D simulations, Sh_x was calculated using the along-tank stress τ_x in the spanwise center of the domain.

Throughout the simulation, the Shields parameter showed that the stress induced by the wave was negative below the leading flank of the wave. In the rear flank, Sh_x was positive until the wave broke ($t \approx 11$ s). Before the rear flank of the wave steepened as breaking began (at $t \approx 10$ s), the maximum magnitude of the Shields parameter remained approximately constant and greater than the typical critical Shields value for bed load transport in unidirectional flows ($|\mathrm{Sh}_x| \approx 0.2 > \mathrm{Sh}_c \approx 0.1$). This is consistent with experiments that showed bed load transport below the leading flank of the ISW shortly after generation. After breaking, the stress (and thus the Shields parameter) became chaotic in the rear of the wave. The stress dampened faster in the 3D simulation compared to the 2D simulation since viscous dissipation acted efficiently in this realistically simulated turbulent flow.

From corresponding experiments, the time and location when resuspension initiates is shown as the point with error bars, where the error bars were calculated from the standard deviation of the time and location of resuspension from repeat experiments. Initiation of resuspension in the experiments aligned spatially and temporally with a spike in the numerically computed Shields parameter and occurred behind the separation point (where $\tau_x = \mathrm{Sh}_x = 0$) and the location of maximum interfacial descent (black curve). In comparing to Figs. 5 and 10, the initiation of resuspension occurred earlier in Fig. 11 because the probe positions chosen to create those figures were located in shallower depths at $x = 100$ cm. A comparison of the 2D and 3D simulations shows that the Sh_x are nearly identical in these configurations until and during wave breaking.

In the study of shoaling internal solitary waves, one might reasonably apply the Shields parameter to predict the onset of bed load transport below the leading flank of the ISW. However, consideration of where the Shields parameter is valid is needed before applying it to particle resuspension. This is because there are two regions of along-slope stress with different dynamics distinguished by the flow separation point. Ahead of the separation point, under the leading flank of the shoaling wave, the descending interface created an opposing vertical flow associated with the descending interface gradually flattening against the bottom slope. This acted to keep particles on the bottom boundary and caused the flow ahead of the separation point to remain stable throughout shoaling, in contrast with the turbulent motions behind the separation point after wave breaking.

From the time series of the 3D simulation in Fig. 11(b), the maximum over the tank bottom of the along-slope Shields parameter $\mathrm{Sh}'_x = \max |\mathrm{Sh}_x|$ was computed. The corresponding across-slope Sh'_y value was also computed. Figure 12 demonstrates that the along-slope stress is sufficient for bed load transport ($\mathrm{Sh}'_x > \mathrm{Sh}_c$), in agreement with observations in the experiments. A rapid increase in Sh'_x occurred during wave breaking ($t \approx 11$) followed by a second increase at $t \approx 15$ when the boundary layer became three dimensional. Particle resuspension, measured from corresponding experiments, occurred mostly after the initial rise in Sh'_x and corresponded to the start of across-slope stress, as seen by Sh'_y. This is in agreement with particle resuspension studies where three-dimensional near-bed eddies typically correlate with particle resuspension.

D. Vertical Lagrangian velocity

Although the experiments and simulations demonstrate that bottom stress plays a role in particle resuspension, the absence of near-bed turbulence during the initiation of resuspension leads us to formulate a diagnostic for resuspension that accounts for boundary layer separation in the lee of the wave.

During shoaling, as shown in Fig. 13, streamlines are nearly parallel to the bottom slope ahead of the separation point and travel away from the separation point afterward. We hypothesize that a particle undergoing bed load transport under the front flank of the wave can be resuspended by following a streamline that deflects away from the bottom near the separation point. Since bed load transport begins under the front flank of the wave ahead of the separation point, many of these particles will tend to be carried along streamlines that are nearly parallel with the bottom ahead of the separation point and will rise rapidly away from the bottom behind the separation point.

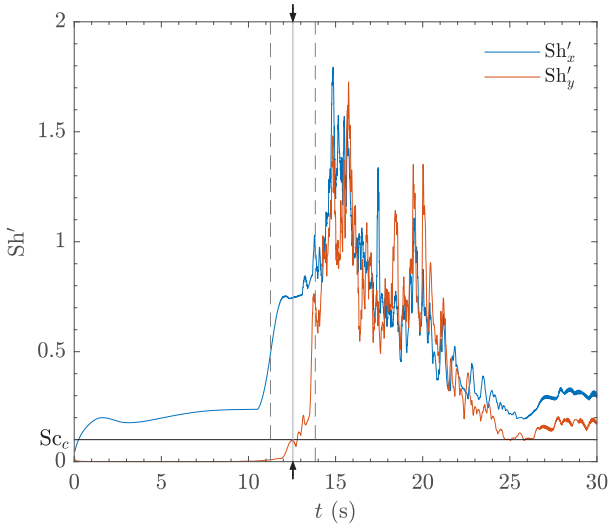

FIG. 12. Maximum Shields parameter in the along-tank Sh'_x and across-tank dimensions Sh'_y for the 3D simulation in Fig. 9. A representative critical Shields parameter for bed load transport of $\mathrm{Sh}_c = 0.1$ is plotted as the horizontal black line. Arrows indicate the time when resuspension begins to occur, as measured in experiments with corresponding error (dashed lines).

To quantify the efficacy of the separating streamline in resuspending particles, we define the vertical Lagrangian velocity

$$w_L = w - su, \tag{3}$$

where u and w are velocities evaluated along a transect parallel to and near the bottom slope. We find that the distance at which w_L is evaluated has a negligible impact on the structure of w_L, regardless of the transect being in the boundary layer or not. Although w_L consists of Eulerian velocities, it is called a Lagrangian velocity because it measures the vertical velocity, relative to the bottom slope, of a fluid parcel following a streamline under the front flank of the wave. Where the flow is parallel to the bottom slope (ahead of the separation point) $w_L = w - su \approx 0$. At the separation point, the change in sign of w results in $w_L > 0$ (since $u < 0$). Since w_L does not include any information about the particles during resuspension, we propose that resuspension occurs if w_L is larger than the particle settling velocity w_s, that is, if

$$w_L/w_s > 1, \tag{4}$$

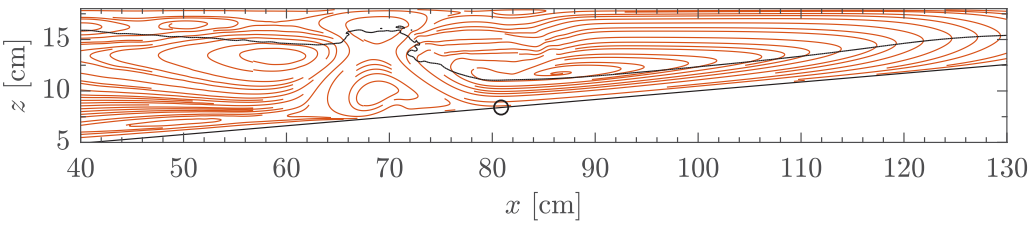

FIG. 13. Snapshot of instantaneous streamlines at $t = 12$ s for the case in Fig. 9. The black line is the location of the pycnocline and the black circle is the separation point. The vertical axis is measured relative to the local base of the tank.

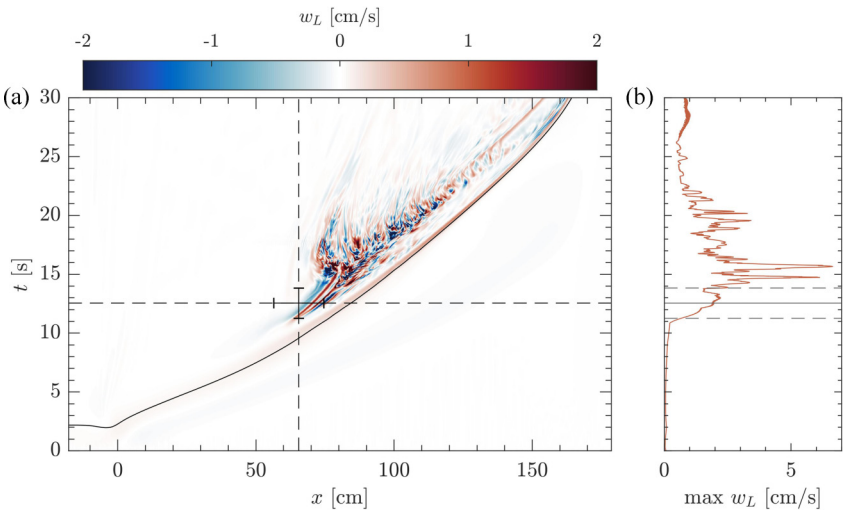

FIG. 14. (a) Time series and (b) maximum vertical Lagrangian velocity w_L at a distance 2 mm above the tank bottom for the 3D case in Fig. 9. The black point with error bars designates the experimental time and position of incipient resuspension. The black line is the location of the separation point along the bottom boundary and is a proxy for the location of the wave crest.

where w_L accounts for the fluid flow and w_s for the properties of the particles. For sufficiently small particles, w_s may be taken as the Stokes settling velocity, though generally it will depend on the particle size, buoyancy, and fluid viscosity.

Boegman and Ivey [26] described a similar mechanism for resuspension caused by flow separation and near-bottom vortices, though they attributed resuspension to viscous and Reynolds stresses. In agreement with what we have just described, the authors found that the viscous stress alone, and thus the use of a Shields parameter, was not a good indicator of resuspension.

Figure 14(a) shows the vertical Lagrangian velocity determined along a transect 2 mm above the bottom for the 3D numerical simulation shown in Fig. 9. The upslope of the separation point (the black curve) w_L is small throughout the simulation, as predicted. Behind the separation point, the magnitude of w_L becomes large after wave breaking at $t \approx 11$ s. The observed location and time when particle resuspension began in the experiments correspond to $w_L \gtrsim w_s \approx 1.9$ cm/s [Fig. 14(b)]; particles with $w_s < 1.9$ cm/s are expected to undergo resuspension earlier. The corresponding experiment showed resuspension to occur over a duration of approximately 9 s, matching the duration of predicted particle resuspension in the simulation, $w_L \gtrsim 1.9$ cm/s. However, the interpretation of w_L corresponding to the vertical Lagrangian velocity along a separating streamline becomes questionable after $t = 15$ s when the near boundary flow becomes chaotic or if the wave encounters strong preexisting bottom boundary layer turbulence.

A comparison of the vertical Lagrangian velocity in Fig. 14(a) to the Shields parameter in Fig. 11(b) shows that the majority of the nonzero component of w_L aligns with where Sh_x is chaotic. This is unsurprising since locations of turbulence or transitional flow will cause variations in both the bottom stress used to calculate Sh and near-bottom velocities used to calculate w_L. Because w_L is defined in terms of near-bottom velocities, it is an easier quantity to measure than the Shields parameter, which requires measurements of the bottom stress.

Having developed a physically justified diagnostic for particle resuspension by shoaling ISWs, we now proceed to predict generally where resuspension should occur as it depends upon the bottom slope and incident ISW characteristics. To this end, a second suite of simulations was initialized with an upstream internal solitary wave specified from a solution of the Dubreil-Jacotin-Long (DJL) equation [41].

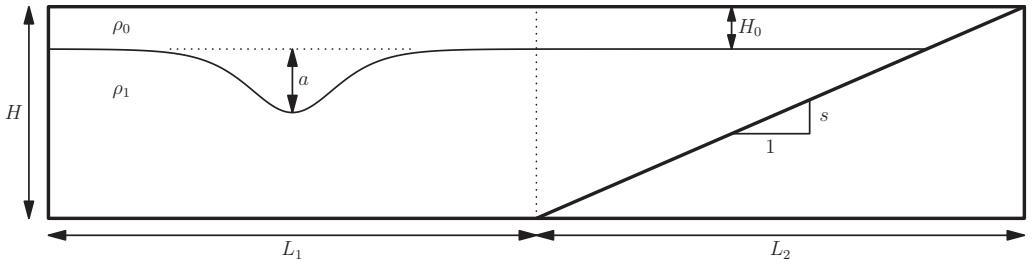

FIG. 15. Schematic of the second simulation domain. The DJL equation was numerically solved in region 1 (of length L_1) and shoaled in region 2 (of length L_2).

These simulations consisted of two parts: (i) numerically solving the DJL equation for an ISW in a rectilinear domain and (ii) time evolving the propagation and shoaling of this wave over a linearly sloped bed (see Fig. 15). The ISWs had a variety of nondimensionalized wave amplitudes a/H_0 which ranged between 0.1 and 5.0 and were set to approach one of three separate slopes $s = 0.01$, 0.05, or 0.10. The DJL equation was numerically solved using a variational formulation using a simple open source MATLAB code [42]. Only 2D simulations were completed because these simulations were designed to study the start of particle resuspension, through the use of Eq. (4), which occurs at the onset of wave breaking.

The fluid depth H was 10 m for all amplitudes except for the case with $a = 5$ m, which had a depth of 20 m to give a more reasonable background depth for the large-amplitude wave before shoaling. A 1-m upper layer H_0 was used. Because these lengths scales are closer to those on a field scale, the wave Reynolds number for this suite of simulations is significantly larger (Re_w between 3×10^4 and 1.5×10^6) than those of the previous simulations and experiments. Although Aghsaee *et al.* [22] pointed out that the dependence of the bottom boundary layer on Reynolds number modifies the shoaling dynamics, we find that there is no impact on the location of the separation point, consistent with their results shown in their Fig. 21. To validate this, a simulation in which all lengths were scaled down by an order of magnitude reproduced the same vertical Lagrangian velocity diagrams up to wave breaking, at which point 2D simulations are no longer applicable. Furthermore, an additional simulation where the pycnocline thickness was doubled resulted in comparable shoaling dynamics. As seen in the previous numerical simulations, wave breaking and $w_L/w_s > 1$ are colocated.

In all large-scale cases, the vertical Lagrangian velocity was measured at distances of 5 and 10 cm above the bottom slope because the domain depth was two orders of magnitude larger than the previous simulations compared against laboratory experiments. The values of w_L at both the 5- and 10-cm transects gave comparable results, suggesting that the distance from the bottom boundary is largely insignificant in determining resuspension. Since the waves were larger than those in the previous simulations, so creating faster near-bed velocities, a value of $w_s = 5$ cm/s was used to evaluate the onset of resuspension through Eq. (4).

The relationship between the incident wave amplitude and the lower layer fluid depth H_r where particle resuspension is observed or predicted to begin is plotted in Fig. 16. For simulations, H_r is computed using the resuspension threshold (4) based on the vertical Lagrangian velocity (blue circles) and also when the Shields parameter surpassed a critical threshold (red triangles) $\mathrm{Sh}'_x > \mathrm{Sh}_c = 1$. These predictions are compared against observations of particle resuspension in the experiments (black crosses in Fig. 16).

Both the experiments and simulations show a linear dependence of the lower layer resuspension depth H_r on the incident wave amplitude a. However, a best-fit line to the simulation predictions gives

$$H_{r,\mathrm{sim}} = 2.06(\pm 0.03)a, \tag{5a}$$

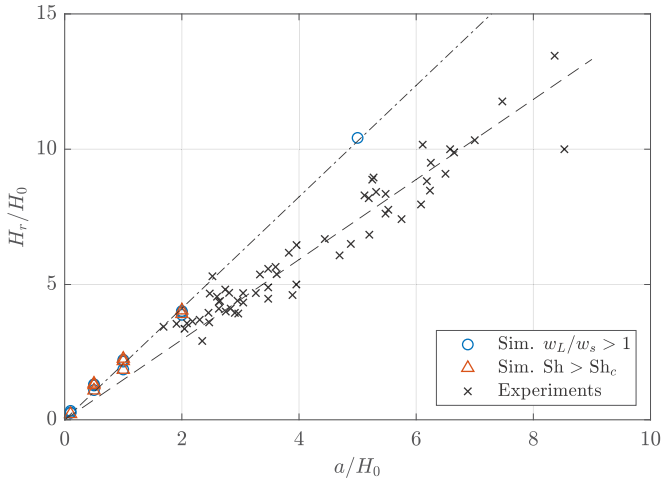

FIG. 16. Resuspension depth versus incident wave amplitude. Here H_r is the lower layer fluid depth when resuspension is predicted to begin in the simulations and is measured from observations in the experiments. Best-fit lines with slopes of 2.06 ± 0.03 (dot-dashed line) and 1.48 ± 0.05 (dashed line) were found for the simulation and experimental data, respectively.

whereas a best-fit line through experimental data gives

$$H_{r,\text{expt}} = 1.48(\pm 0.05)a. \tag{5b}$$

The discrepancy between simulations and experiments may be attributed in part to uncertainties in the measured locations of resuspension and also to uncertainties of the particle densities used in the experiments. In experiments, it was particularly difficult to determine the moment at which particle resuspension began. As such, a conservative estimate was made by characterizing resuspension as when a significant number of particles were seen to rise from the bottom boundary. This would necessarily occur later in time and in shallower fluid compared to when the first particle was resuspended.

Note that Eqs. (5) do not include the depth of the upper layer. The more applicable variable for oceanographers is the total fluid depth which can be calculated by simply adding the upper layer depth $H_{r,\text{tot}} = H_r + H_0$.

In simulations and experiments of shoaling ISWs on linear slopes without particles, Aghsaee *et al.* [22] and Helfrich [43] found that wave breaking occurred when H_r/a was between 2 and 3. Our results, by comparison, show that particle resuspension occurs in shallower fluid after the wave breaks. In spite of the difference between the numerical and experimental results, the consistency of the resuspension criterion over a range of bottom slopes shows it to be robust for a wide range of breaking behaviors.

V. DISCUSSION AND CONCLUSIONS

Motivated by the desire to quantify where and when shoaling internal solitary waves cause resuspension, we performed both laboratory experiments and numerical simulations. The experiments and some of the simulations used the lock-release mechanism to form ISWs which then shoaled onto the sloping bottom. The ISWs were of large amplitude, up to 8 times the characteristic depth $\bar{H}$, such that they were well into the nonlinear regime.

Excellent agreement was found in the structure of the velocity fields between the numerical simulations and the laboratory experiments, the former of which shows a separation point followed by a burst of vertical motion near the bottom boundary. Boegman and Ivey [26] suggested that it is this burst of vertical motion that causes particle resuspension.

To quantify the connection between separation and vertical motion, we proposed a simple criterion based on the deflection of a streamline near a separation point to predict the location of initial particle resuspension. From this criterion, a second set of simulations and the experiments showed that particle resuspension is predicted to begin when the ratio of the lower layer fluid depth and incident wave amplitude is between 1.5 and 2.

As an example of the application of our results, we consider observations of shoaling ISW in the South China Sea where the bottom slope [44] is around 0.01. Incident wave amplitudes in this region [3] are typically 100–200 m, and the thermocline is at a depth of approximately 100 m. From (5b) we predict that particle resuspension should occur at fluid depths between 250 and 400 m. Indeed, observations [44] show large deep water sand dunes in depths ranging between 160 and 600 m. In addition to the formation of dunes, thick nepheloid layers suspected of forming from shoaling ISWs have been found [4] at depths up to 1500 m. Lien *et al.* [45] observed a nepheloid layer arising from sediment resuspension at a depth of 400 m due to the shoaling of a wave with an amplitude of 200 m and an upper layer depth of 100 m. Our predicted depth of resuspension (also 400 m) agrees remarkably well with this observation.

Particle resuspension is not limited to shoaling internal waves alone and may occur due to global instabilities caused by strong nonlinear waves traveling on a flat bottom [46–48]. However, for this instability to develop, a critical Reynolds number must be surpassed [38]. As mentioned previously, the Reynolds number adjusts the dynamics of shoaling ISWs but does not appear to change the location of the onset of particle resuspension nor does there appear to be a critical value necessary for resuspension. It is expected that the magnitude of particle resuspension will be Reynolds numbers dependent, but this requires further validation, specifically in how it affects the stability of the boundary layer in the presence of turbulence. Three-dimensional simulations of a turbulent bottom boundary layer are currently accessible and will assess the wider applicability of the vertical Lagrangian velocity to resuspension in more chaotic environments. Consideration of different breaking types is also needed for further validation.

In deep waters, Olsthoorn *et al.* [49] and Rivera-Rosario *et al.* [48] showed that wave-induced pressure at the bed can cause nutrient seepage and bed failure. These authors emphasized the significant role that bed composition plays in the sensitivity of the bed to external flows. Like Aghsaee and Boegman [47], Rivera-Rosario *et al.* [48] modified the Shields parameter to account for an increase in the buoyancy of bottom material due to the wave-induced pressure gradient. Rather than following this approach, we introduced the vertical Lagrangian velocity as a means to account for the velocity signature of the trailing adverse pressure gradient.

Although mustard seeds proved useful in demonstrating bed load transport, flow separation, and particle resuspension, they are an idealization of true ocean floor sediment which may consist of particles of different size, shape, density, and cohesion. Properly accounting for these parameters will prove difficult in laboratory experiments and numerical simulations, but will further enhance our understanding of seabed transformation due to shoaling internal waves.

As often seen in particle transport studies, the Shields parameter showed a correlation between heightened bottom stress and particle resuspension. Therefore, it is in locations of high stress where care is needed in designing offshore structures where particle transport is expected to be the greatest. Our results suggest that particular focus should be upon depths where the lower layer is between 1.5 and 2 times the incident ISW amplitude.

We have focused on where resuspension begins to occur due to shoaling internal solitary waves. Further investigation into the duration of resuspension and the consequent redistribution of sediment due to shoaling waves is needed.

ACKNOWLEDGMENTS

This research was in part supported by the Natural Sciences and Engineering Research Council of Canada (NSERC) Discovery under Grant No. RGPIN-2015-04758. The authors acknowledge Compute Canada's high performance computing cluster Graham, on which simulations were completed.

[1] *Nonlinear Internal Waves in Lakes*, edited by K. Hutter, Advances in Geophysical and Environmental Mechanics and Mathematics (Springer, Berlin, 2012).
[2] M. H. Orr and P. C. Mignerey, Nonlinear internal waves in the south china sea: Observation of the conversion of depression internal waves to elevation internal waves, J. Geophys. Res.: Oceans **108**, 3064 (2003).
[3] M. H. Alford, T. Peacock, J. A. MacKinnon, J. D. Nash, M. C. Buijsman, L. R. Centurioni, S.-Y. Chao, M.-H. Chang, D. M. Farmer, O. B. Fringer *et al.*, The formation and fate of internal waves in the South China Sea, Nature (London) **521**, 65 (2015).
[4] Y. Jia, Z. Tian, X. Shi, J. Liu, J. Chen, X. Liu, R. Ye, Z. Ren, and J. Tian, Deep-sea sediment resuspension by internal solitary waves in the northern South China Sea, Sci. Rep. **9**, 12137 (2019).
[5] J. Belde, S. Back, and L. Reuning, Three-dimensional seismic analysis of sediment waves and related geomorphological features on a carbonate shelf exposed to large amplitude internal waves, Browse Basin region, Australia, Sedimentology **62**, 87 (2015).
[6] M. D. Rayson, N. L. Jones, and G. N. Ivey, Observations of large-amplitude mode-2 nonlinear internal waves on the Australian north west shelf, J. Phys. Oceanogr. **49**, 309 (2019).
[7] J. M. Klymak and J. N. Moum, Internal solitary waves of elevation advancing on a shoaling shelf, Geophys. Res. Lett. **30**, 2045 (2003).
[8] J. N. Moum, J. M. Klymak, J. D. Nash, A. Perlin, and W. D. Smyth, Energy transport by nonlinear internal waves, J. Phys. Oceanogr. **37**, 1968 (2007).
[9] S. Zhang, M. H. Alford, and J. B. Mickett, Characteristics, generation and mass transport of nonlinear internal waves on the Washington continental shelf, J. Geophys. Res.: Oceans **120**, 741 (2015).
[10] C. H. Mortimer, Lake hydrodynamics, SIL Commun. **20**, 124 (1974).
[11] V. I. Vlasenko and K. Hutter, Transformation and disintegration of strongly nonlinear internal waves by topography in stratified lakes, Ann. Geophys. **20**, 2087 (2002).
[12] W. Eckert, J. Imberger, and A. Saggio, Biogeochemical response to physical forcing in the water column of a warm monomictic lake, Biogeochemistry **61**, 291 (2002).
[13] B. J. Wang, D. J. Bogucki, and L. G. Redekopp, Internal solitary waves in a structured thermocline with implications for resuspension and the formation of thin particle-laden layers, J. Geophys. Res.: Oceans **106**, 9565 (2001).
[14] D. J. Bogucki, L. G. Redekopp, and J. Barth, Internal solitary waves in the Coastal Mixing and Optics 1996 experiment: Multimodal structure and resuspension, J. Geophys. Res. **110**, C02024 (2005).
[15] D. Bourgault, M. Morsilli, C. Richards, U. Neumeier, and D. E. Kelley, Sediment resuspension and nepheloid layers induced by long internal solitary waves shoaling orthogonally on uniform slopes, Cont. Shelf Res. **72**, 21 (2014).
[16] B. Butman, P. S. Alexander, A. Scotti, R. C. Beardsley, and S. P. Anderson, Large internal waves in Massachusetts Bay transport sediments offshore, Cont. Shelf Res. **26**, 2029 (2006).
[17] W. Zhang, I. Didenkulova, O. Kurkina, Y. Cui, J. Haberkern, R. Aepfler, A. I. Santos, H. Zhang, and T. J. J. Hanebuth, Internal solitary waves control offshore extension of mud depocenters on the NW Iberian shelf, Mar. Geol. **409**, 15 (2019).
[18] L. Boegman and M. Stastna, Sediment resuspension and transport by internal solitary waves, Annu. Rev. Fluid Mech. **51**, 129 (2019).
[19] Y. Sakai, J. Murase, A. Sugimoto, K. Okubo, and E. Nakayama, Resuspension of bottom sediment by an internal wave in Lake Biwa, Lake Reserv. Manage. **7**, 339 (2002).
[20] A. Shields, Anwendung der aehnlichkeitsmechanick und der turbulenzforschung auf die geschiebebewegung, Mitt. Preuss. Vers. Wasser. Schiff. **26**, 1 (1936).
[21] L. Boegman, G. N. Ivey, and J. Imberger, The degeneration of internal waves in lakes with sloping topography, Limnol. Oceanogr. **50**, 1620 (2005).
[22] P. Aghsaee, L. Boegman, and K. G. Lamb, Breaking of shoaling internal solitary waves, J. Fluid Mech. **659**, 289 (2010).
[23] K. Nakayama, T. Sato, K. Shimizu, and L. Boegman, Classification of internal solitary wave breaking over a slope, Phys. Rev. Fluids **4**, 014801 (2019).

[24] D. J. Bogucki and L. G. Redekopp, A mechanism for sediment resuspension by internal solitary waves, Geophys. Res. Lett. **26**, 1317 (1999).
[25] P. Aghsaee, L. Boegman, P. J. Diamessis, and K. G. Lamb, Boundary-layer-separation-driven vortex shedding beneath internal solitary waves of depression, J. Fluid Mech. **690**, 321 (2012).
[26] L. Boegman and G. N. Ivey, Flow separation and resuspension beneath shoaling nonlinear internal waves, J. Geophys. Res. **114**, C02018 (2009).
[27] R. S. Arthur and O. B. Fringer, Transport by breaking internal gravity waves on slopes, J. Fluid Mech. **789**, 93 (2016).
[28] E. Masunaga, R. S. Arthur, O. B. Fringer, and H. Yamazaki, Sediment resuspension and the generation of intermediate nepheloid layers by shoaling internal bores, J. Mar. Syst. **170**, 31 (2017).
[29] B. R. Sutherland, K. J. Barrett, and G. N. Ivey, Shoaling internal solitary waves, J. Geophys. Res. **118**, 4111 (2013).
[30] L. F. Pratson and W. F. Haxby, What is the slope of the U.S. continental slope? Geology **24**, 3 (1996).
[31] D. B. O'Grady, J. P. M. Syvitski, L. F. Pratson, and J. F. Sarg, Categorizing the morphologic variability of siliciclastic passive continental margins, Geology **28**, 207 (2000).
[32] K. Hunkins and M. Fliegel, Internal undular surges in seneca lake: A natural occurrence of solitons, J. Geophys. Res. **78**, 539 (1973).
[33] R. C. Wiegand and E. C. Carmack, The climatology of internal waves in a deep temperate lake, J. Geophys. Res.: Oceans **91**, 3951 (1986).
[34] See Supplemental Material at http://link.aps.org/supplemental/10.1103/PhysRevFluids.5.054303 for corresponding videos.
[35] C. D. Moore, J. R. Koseff, and E. L. Hult, Characteristics of bolus formation and propagation from breaking internal waves on shelf slopes, J. Fluid Mech. **791**, 260 (2016).
[36] Z. Tian, X. Guo, L. Qiao, Y. Jia, and L. Yu, Experimental investigation of slope sediment resuspension characteristics and influencing factors beneath the internal solitary wave-breaking process, Bull. Eng. Geol. Environ. **78**, 959 (2019).
[37] P. J. Diamessis and L. G. Redekopp, Numerical investigation of solitary internal wave-induced global instability in shallow water benthic boundary layers, J. Phys. Oceanogr. **36**, 784 (2006).
[38] M. Carr, P. A. Davies, and P. Shivaram, Experimental evidence of internal solitary wave-induced global instability in shallow water benthic boundary layers, Phys. Fluids **20**, 066603 (2008).
[39] C. J. Subich, K. G. Lamb, and M. Stastna, Simulation of the Navier-Stokes equations in three dimensions with a spectral collocation method, Int. J. Numer. Methods Fluids **73**, 103 (2013).
[40] L. C. van Rijn, Sediment transport, Part I: Bed load transport, J. Hydraul. Eng. **110**, 1431 (1984).
[41] K. G. Lamb, A numerical investigation of solitary internal waves with trapped cores via shoaling, J. Fluid Mech. **451**, 109 (2002).
[42] M. Dunphy, C. Subich, and M. Stastna, Spectral methods for internal waves: indistinguishable density profiles and double-humped solitary waves, Nonlin. Process. Geophys. **18**, 351 (2011).
[43] K. R. Helfrich, Internal solitary wave breaking and run-up on a uniform slope, J. Fluid Mech. **243**, 133 (1992).
[44] D. B. Reeder, B. B. Ma, and Y. J. Yang, Very large subaqueous sand dunes on the upper continental slope in the South China Sea generated by episodic, shoaling deep-water internal solitary waves, Mar. Geol. **279**, 12 (2011).
[45] R.-C. Lien, F. Henyey, and B. Ma, Large-amplitude internal solitary waves observed in the northern South China Sea: Properties and energetics, J. Phys. Oceanogr. **44**, 1095 (2014).
[46] L. S. Quaresma, J. Vitorino, A. Oliveira, and J. da Silva, Evidence of sediment resuspension by nonlinear internal waves on the western Portuguese mid-shelf, Mar. Geol. **246**, 123 (2007).
[47] P. Aghsaee and L. Boegman, Experimental investigation of sediment resuspension beneath internal solitary waves of depression, J. Geophys. Res.: Oceans **120**, 3301 (2015).
[48] G. A. Rivera-Rosario, P. J. Diamessis, and J. T. Jenkins, Bed failure induced by internal solitary waves, J. Geophys. Res.: Oceans **122**, 5468 (2017).
[49] J. Olsthoorn, M. Stastna, and N. Soontiens, Fluid circulation and seepage in lake sediment due to propagating and trapped internal waves, Water Resour. Res. **48**, W11520 (2012).